

# Rapid and Surfactant-Free Synthesis of Bimetallic Pt–Cu Nanoparticles Simply via Ultrasound-Assisted Redox Replacement

Zhenyu Sun,<sup>†</sup> Justus Masa,<sup>‡</sup> Wei Xia,<sup>†</sup> Dennis König,<sup>§</sup> Alfred Ludwig,<sup>§</sup> Zi-An Li,<sup>⊥</sup> Michael Farle,<sup>⊥</sup> Wolfgang Schuhmann,<sup>‡</sup> and Martin Muhler<sup>\*†</sup>

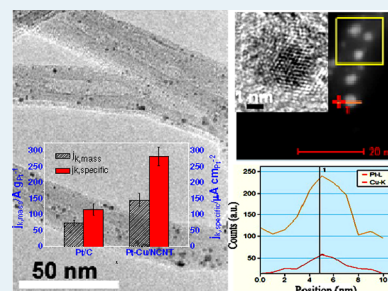
<sup>†</sup>Laboratory of Industrial Chemistry, <sup>‡</sup>Analytische Chemie-Elektroanalytik & Sensorik, <sup>§</sup>Department of Mechanical Engineering, Institute for Materials, Ruhr-University Bochum, D-44780 Bochum, Germany

<sup>⊥</sup>Fakultät für Physik and CeNIDE, Universität Duisburg-Essen, Lotharstrasse 1, D-47057 Duisburg, Germany

## S Supporting Information

**ABSTRACT:** The synthesis of bimetallic nanoparticles (NPs) with well-defined morphology and a size of <5 nm remains an ongoing challenge. Here, we developed a facile and efficient approach to the design of bimetallic nanostructures by the galvanic replacement reaction facilitated by high-intensity ultrasound (100 W, 20 kHz) at low temperatures. As a model system, Pt–Cu NPs deposited on nitrogen-doped carbon nanotubes (NCNTs) were synthesized and characterized by spectroscopic and microscopic techniques. Transmission electron microscopy (TEM) inspection shows that the mean diameter of Pt–Cu NPs can be as low as  $\approx 2.8$  nm, regardless of the much larger initial Cu particle size, and that a significant increase in particle number density by a factor of 35 had occurred during the replacement process. The concentration of the Pt precursor solution as well as of the size of the seed particles were found to control the size of the bimetallic NPs. Energy dispersive X-ray spectroscopy performed in the scanning TEM mode confirmed the alloyed nature of the Pt–Cu NPs. Electrochemical oxygen reduction measurements demonstrated that the resulting Pt–Cu/NCNT catalysts exhibit an approximately 2-fold enhancement in both mass- and area-related activities compared with a commercial Pt/C catalyst.

**KEYWORDS:** Pt–Cu, alloy, ultrasonication, redox replacement, oxygen reduction reaction



## INTRODUCTION

Bimetallic nanoparticles (NPs) exhibit novel multifunctional and enhanced synergistic properties that make them advantageous over monometallic counterparts for a range of fundamental studies and applications.<sup>1–13</sup> For example, bimetallic NPs usually demonstrate remarkably high catalytic activities for different chemical processes, which are ascribed to electronic (ligand) effects or geometric effects (or both) caused by the surface atomic environment of distinct metal atoms.<sup>1,10</sup> In particular, alloying Pt with nonprecious metals, such as Fe, Co, or Ni, enables a 2–10 fold improvement in oxygen reduction reaction activity relative to pure Pt showing a great potential in proton exchange membrane fuel cells.<sup>1–3,5,8,11,12,14</sup> For the purpose of better tailoring their activities and understanding the correlation between their structures and properties, control over the composition, shape, and architecture of bimetallic systems is critically important.

To date, the synthesis of bimetallic NPs with well-defined morphology and a size of less than 5 nm remains a challenge. One major scheme is applied in the gas phase; the other, in the liquid phase. The gas-phase strategy includes flame pyrolysis,<sup>15</sup> laser ablation,<sup>16</sup> and chemical vapor deposition.<sup>17</sup> The processing procedures of these methods are often complex and require harsh conditions, such as high temperature, resulting in excessive particle growth and severe particle

aggregation. The solution-phase protocol mainly involves colloidal synthesis, that is, the reduction of two metal precursor solutions by a chemical reducing agent either simultaneously<sup>10</sup> or sequentially,<sup>9</sup> and electrochemical approaches, including both the under potential deposition followed by redox replacement<sup>18,19</sup> and dealloying<sup>2,6</sup> methods. The colloidal strategy tends to produce NPs with random architectures and polydispersed size distributions due to different reduction potentials for the individual metal ions.<sup>20</sup> Stabilizing ligands (i.e., organic species, surfactants) are usually required in both cases for the control of particle nucleation and growth, and as a result, impurities may be introduced in the final product, which must be removed afterward for many applications. Therefore, it would be of particular interest to develop simpler approaches operating at mild conditions with low amounts of impurities and allowing greater control over particle size and atomic distribution.

Use of sonication results in unique advantages in many chemical processes, particularly in the synthesis of novel electrochemically active nanoparticles.<sup>21–25</sup> Ultrasound waves are known to consist of compression and rarefaction cycles.

Received: March 21, 2012

Revised: June 27, 2012

Published: June 28, 2012

Cavitation takes place during rarefaction cycles, in which the negative acoustic pressure is sufficiently large to rupture the liquid, creating stable or transient cavitation bubbles.<sup>24</sup> In the case of transient cavitation, bubbles grow within a short period of time and collapse violently, generating shock waves. Unusual sonochemical effects are induced, including the formation of radicals and the enhancement of reaction rates at ambient conditions.<sup>24</sup> Ultrasonic intensity and sonication time are important parameters affecting the formation of nanomaterials. Microturbulence and collapsing bubbles both on the surface and in the liquid close to a surface, forming microjets, facilitate the collision of reactive species (pitting effect), thus enhancing surface reactivity. They can also provide mechanical energy to overcome the attractive forces between bundles or layered structures, leading to their exfoliation and dispersion.<sup>26</sup>

Here, we demonstrate that the redox replacement reaction can be greatly facilitated by high-intensity ultrasound, which otherwise proceeds slowly at  $T \approx 0$  °C. This finding offers a facile, rapid, and green route for the design of bimetallic NPs based on solution-phase chemistry without electrochemical treatments. Note that no capping ligands are required during the process, resulting in clean surfaces for the NPs and avoiding the problem that the stabilizer molecules adversely affect particle properties. The size of the seed NPs can be readily tuned by controlling their loading level on nitrogen-doped carbon nanotubes (NCNTs), ultrasonic intensity, and precursor concentration. Coupled with tuning of the concentration of the oxidizing precursor, bimetallic NPs with controlled size and composition can be fabricated. To gain insight into the application of bimetallic NPs in catalysis, NCNTs were used as support for metal NP immobilization because of their large surface area, high mechanical strength, and outstanding electrical conductivity. The electrocatalytic activity of the resulting catalyst was investigated with respect to the oxygen reduction reaction (ORR).

## EXPERIMENTAL SECTION

**Materials.** All chemicals used in this work were of analytical grade and used as supplied.  $\text{Cu}(\text{NO}_3)_2 \cdot 3\text{H}_2\text{O}$  and  $\text{AgNO}_3$  were obtained from Sigma-Aldrich.  $\text{Pt}(\text{NO}_3)_2$  and  $\text{Pd}(\text{O}_2\text{CCH}_3)_2$  were provided by Chempur Feinchemikalien and Forschungsbedarf and ABCR, respectively. High-purity ( $\geq 95\%$ ) carbon nanotubes (CNTs) with inner mean diameter of  $\approx 4$  nm and outer mean diameter of  $\approx 13$  nm were supplied by Bayer Material Science. The as-received CNTs were first oxidized via  $\text{HNO}_3$  vapor treatment at 200 °C for 48 h.<sup>27</sup> After cooling and repeated washing with distilled water, the CNTs were dried at 60 °C overnight. Then, 200 mg of the oxidized CNTs was subjected to heating in 10 vol %  $\text{NH}_3$  in He at a flow rate of 25 sccm at 400 °C for 6 h to generate N-containing functional groups.<sup>28</sup>

**Synthesis of Bimetallic NPs Deposited on NCNTs.** The sonochemical system used in this work is illustrated in Figure S1a of the Supporting Information. The ultrasonic power ( $P$ ) was estimated by calorimetric measurements using the equation  $P = mC_{\text{H}_2\text{O}}\Delta T/t$ , where  $m$  is the mass of water,  $C_{\text{H}_2\text{O}}$  is the heat capacity of water ( $4.18 \text{ J g}^{-1} \text{ K}^{-1}$ ),  $\Delta T$  corresponds to the resulting temperature rise, and  $t$  represents the sonication time. Supporting Information Figure S1b shows the electrical power as a function of ultrasonic power for the system used in this work. The ultrasonic intensity ( $\text{W cm}^{-2}$ ) was calculated from the ultrasonic power divided by the surface area of the tip ( $\pi r^2$ ).

Typically, 2.5 mg of NCNTs was initially dispersed in 20 mL of an aqueous solution of the precursor (except an acetate solution for  $\text{Pd}(\text{O}_2\text{CCH}_3)_2$ ) at a designated concentration to form a uniform suspension with the aid of tip sonication (Bandelin Sonoplus HD3100, 100 W, 20 kHz, 13 mm diameter tip) for 2 min. As 1 mL of a  $\text{NaBH}_4$  aqueous solution with a concentration 5 times higher than that of the precursor was added dropwise into the dispersion containing metal precursor under tip sonication within 2 min, seed metal NPs were produced and deposited onto the NCNTs. The precipitate was collected via repeated washing with distilled water, followed by ultracentrifugation to remove excessive  $\text{NaBH}_4$  and then redispersed into 20 mL of water by 2 min tip sonication. Subsequently, an aqueous solution of the second metal precursor with higher reduction potential was added dropwise into the above suspension under tip sonication within 3 min. All the synthetic processes were conducted under an Ar atmosphere in an ice–water bath ( $\approx 0$  °C). The obtained system was ultracentrifuged, and the collected precipitate was first washed thoroughly with distilled water and then vacuum-dried at 60 °C for 6 h.

**Characterization.** X-ray diffraction (XRD) was performed with a D/MAX-RC diffractometer operated at 30 kV and 100 mA with Cu  $K\alpha$  radiation. XPS measurements were carried out in an ESCA Lab 220i-XL spectrometer at a pressure of  $\approx 3 \times 10^{-9}$  mbar (1 mbar = 100 Pa) using Al  $K\alpha$  as the excitation source ( $h\nu = 1486.6$  eV) and operated at 15 kV and 20 mA. SEM observation was carried out on a field emission microscope (FEI Quanta 600 FEG) operated at 20 kV. TEM and high-resolution TEM measurements were made using a transmission electron microscope (FEI Tecnai F20) operated at 200 kV and equipped with an energy-dispersive X-ray spectrometer (EDX) and a high-angle annular dark-field (HAADF) detector.

**Electrochemical Studies.** Electrochemical measurements were performed using a potentiostat/galvanostat (Autolab; Eco Chemie,) supported by NOVA 1.6 software. For rotating disk electrode (RDE) measurements, a rotator EDI 101 and its control unit CTV101 (Radiometer) were used. Electrocatalytic ORR measurements were performed in a single compartment glass cell using glassy carbon ( $\varnothing$  4 mm; HTW) modified with a catalyst film as the working electrode, a platinum wire as the counter electrode, and a reversible hydrogen electrode (RHE) as the reference electrode. For all catalysts investigated in this study, a catalyst ink was formed by dispersing 2.5 mg of the catalyst powder in a mixture of ethanol and water (1:1 volume ratio) and sonicating the mixture for 15 min. A 5.3  $\mu\text{L}$  portion of the resulting homogenized suspension was carefully pipetted onto a finely polished glassy carbon electrode and allowed to dry in air for at least 30 min. For the ORR measurements, the electrolyte was first saturated with argon to record background currents and later saturated with oxygen by purging a stream of oxygen through the electrolyte for at least 20 min. Electrocatalytic ORR currents were obtained by subtracting the background currents from the currents recorded under oxygen-saturated conditions.

## RESULTS AND DISCUSSION

Galvanic metal exchange reactions offer a simple way to prepare bimetallic nanostructures using various transition metals as sacrificial templates.<sup>29–31</sup> Although the relative reduction potential (RP) levels rationalize electron transfer from a metal with lower RP ( $\text{Cu}^{2+}/\text{Cu}$ ,  $E^0 = +0.340$  V vs NHE) to

metal ions with higher RP ( $\text{Pt}^{2+}/\text{Pt}$ ,  $E^0 = +1.118$  V vs NHE), thereby enabling their reduction by the galvanic displacement reaction ( $\text{Cu} + \text{Pt}^{2+} \rightarrow \text{Cu}^{2+} + \text{Pt}$ ), it is important to address how this thermodynamically favorable chemical process occurs at low temperatures. To this end, Cu NPs decorated on NCNTs were initially prepared via a sonication-facilitated deposition method and subsequently mixed with an aqueous solution of  $\text{Pt}(\text{NO}_3)_2$  by magnetic stirring or tip sonication. It was surprising to find that the displacement of Cu by  $\text{Pt}^{2+}$  took place after being subjected to 3 min high-intensity ultrasonic irradiation at  $T \approx 0$  °C, but this was not the case for magnetic stirring under otherwise identical experimental conditions.

As can be seen from the UV–visible absorption spectra of the supernatants obtained after centrifugation (Figure 1), the

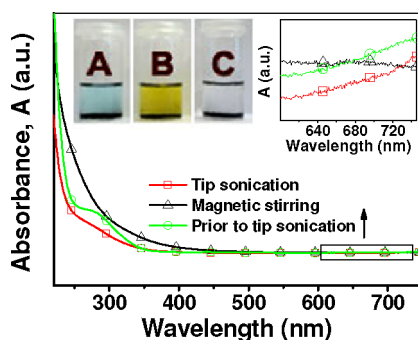


**Figure 1.** UV–vis absorption spectra of the supernatants of the suspensions after centrifugation obtained from the starting material consisting of NCNTs dispersed in aqueous  $\text{Cu}(\text{NO}_3)_2$  solution (A, upper left inset), and from the replacement of Cu by  $\text{Pt}^{2+}$  under magnetic stirring (B, upper left inset) and intensive tip sonication (C, upper left inset), respectively.

onset of a broad absorption band typical of  $\text{Cu}^{2+}$  appeared in the range 600–800 nm in the case of ultrasonication indicating the occurrence of reduction,<sup>32</sup> whereas no clearly resolved signal was observed under magnetic stirring. This hypothesis is supported by the color change of the suspensions, as displayed in the inset of Figure 1. For comparison, an aqueous solution of pure  $\text{Pt}(\text{NO}_3)_2$  was subjected to a similar sonication treatment, and virtually no Pt-related precipitate was formed in that way. Consequently, it is not likely that depletion of the precursor resulted from its direct decomposition or reduction aided by ultrasonic power. All these results strongly suggest that highly intensive sonication greatly promoted the redox replacement reaction at low temperatures that was hardly realized under conventional agitation.

An extension of this sonication-facilitated displacement scenario permits the rational fabrication of hierarchical structures. For instance, bimetallic Pt–Cu NPs were produced using presynthesized Cu NPs as a sacrificial template with the aid of ultrasound irradiation at  $T \approx 0$  °C. Figure 2 shows representative XRD patterns for Cu/NCNT and Pt–Cu/NCNT. The strong diffraction peak at  $25.9^\circ$  shown in traces A and B in Figure 2 originates from the (002) reflection of the graphitic structure of the multiwalled NCNTs.<sup>33</sup> In trace A, the additional peak at  $43.3^\circ$  can be indexed as the (111) reflection of the Cu face-centered cubic (fcc) phase (JCPDS file 85-1326), the position of which is shifted toward lower  $2\theta$  for the Pt–Cu/NCNT sample, as shown in trace B. Note that the typical diffraction peaks of fcc Pt were not observed, implying that Pt may exist mainly as Pt–Cu alloys in the bimetallic

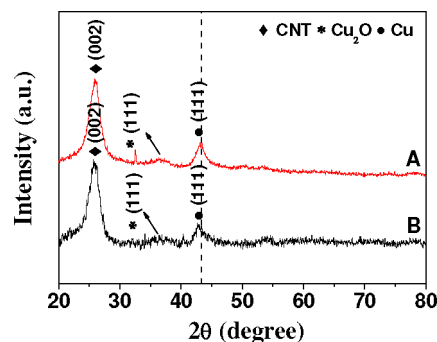


**Figure 2.** XRD patterns of Cu/NCNT (trace A) and Pt–Cu/NCNT (trace B); the dashed line denotes the (111) reflection of pure Cu.

structure. There is a relatively weak diffraction peak at  $36.6^\circ$  in both patterns, corresponding to the (111) reflection of cubic  $\text{Cu}_2\text{O}$  (JCPDS file 78–2076), which might be ascribed to the occurrence of  $\text{Cu}^0$  oxidation upon exposure of the sample to ambient air.

The unit-cell parameter  $a$  for the resultant Pt–Cu can be calculated to be  $3.669$  Å from the lattice spacing for the (111) peak ( $d_{111}$ ) by  $a = \sqrt{3} d_{111} = \sqrt{3} \lambda / (2 \sin(\theta))$ , where  $\lambda$  is the wavelength of the X-rays ( $0.154$  nm) and  $\theta$  is the Bragg angle. This contrasts with the value  $3.619$  Å for pure Cu. The Pt/Cu atom ratio was  $16:84$  as determined according to Vegard's law<sup>34</sup> by  $a = a_0 + kx_{\text{Pt}}$ , where  $a_0$  is the unit-cell parameter of pure Cu,  $x_{\text{Pt}}$  is the molar ratio of Pt in the bimetallic phase, and  $k$  is a constant ( $\approx 0.308$  Å for Pt–Cu systems). This approximation, which deviates from the bulk analysis data ( $\text{Pt}_{34}\text{Cu}_{66}$ ) obtained by atomic emission spectrometry with inductively coupled plasma (ICP-AES), may suggest the presence of other architectures of Pt–Cu NPs in addition to alloys. The average crystallite size was estimated as  $2.9$  nm from the (111) reflection utilizing Scherrer's equation relating the coherently scattering domains with Bragg peak widths:  $L = k\lambda/B \cos(\theta)$ , where  $k = 0.89$  for spherical particles and  $B$  is the full angular width at half-maximum of the peak in radians.

XPS was employed to provide insight into the surface composition of the resulting Pt–Cu/NCNT sample. Supporting Information Figure S2a shows the Pt 4f XPS spectrum, which consists of asymmetric Pt  $4f_{7/2}$  and  $4f_{5/2}$  peaks centered at  $72.2$  and  $75.5$  eV, respectively. The Pt  $4f_{7/2}$  binding energy (BE) of Pt–Cu/NCNT is shifted to a higher value compared with the BE of Pt foil amounting to  $70.7$  eV. The reason for this shift is unclear at present. It probably originates from the combination of size effect and charge transfer from Pt–Cu to the NCNT support.<sup>35</sup> The Cu 2p XPS spectrum (Supporting Information Figure S2b) exhibited peaks at  $932.4$  (Cu  $2p_{3/2}$ ) and  $952.1$  eV (Cu  $2p_{1/2}$ ), indicative of  $\text{Cu}^0$  or  $\text{Cu}^+$  (or both).<sup>36</sup> On the basis of the XRD data shown in Figure 2, it is most likely that Cu exists predominantly in the metallic state. Unfortunately,  $\text{Cu}^+$  cannot be distinguished from  $\text{Cu}^0$  by XPS because of their overlapping Cu 2p spectra. The other weaker doublets at higher binding energies displayed in Supporting Information Figure S2a, b are associated with  $\text{Pt}^{2+}$  and  $\text{Cu}^{2+}$ , respectively, which may result from the slight oxidation of the corresponding metal in contact with air.

No free-standing particles detached from the NCNTs, large NP aggregates, or agglomerates were observed during SEM imaging of the sample (Figure 3a). The formation of highly dispersed Pt–Cu NPs was confirmed by in situ EDX (inset of

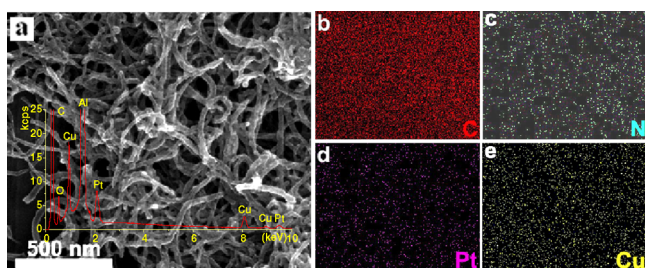


**Figure 3.** (a) SEM image of Pt–Cu/NCNTs (inset: EDX pattern of the sample). (b–e) EDX mapping images of C, N, Pt, and Cu, respectively, taken from the regime shown in panel a.

Figure 3a) together with elemental mapping (Figure 3b–e). Quantitative SEM-EDX analysis (Supporting Information Table S1) yielded the stoichiometric composition of the bimetallic phase as  $\text{Pt}_{35}\text{Cu}_{65}$ , matching well with that of  $\text{Pt}_{34}\text{Cu}_{66}$  determined by ICP-AES. TEM observations for 20 different sample areas show that NPs with high uniformity in diameter remained well dispersed on the NCNTs, even after the displacement reaction (Figure 4a, b). A TEM image of the

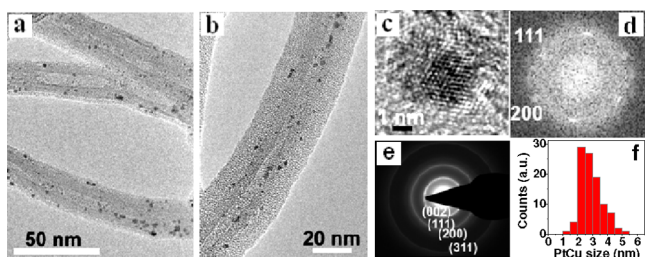


**Figure 4.** TEM images of (a) several individual Pt–Cu/NCNTs and (b) a single Pt–Cu/NCNT. (c) HRTEM image of a NP deposited on NCNTs. (d) FFT analysis of the NP displayed in panel c. (e) Electron diffraction pattern of the Pt–Cu/NCNTs taken from the circled regime shown in Supporting Information Figure S3b. (f) Size distribution of Pt–Cu NPs.

seed Cu NPs supported on NCNTs is shown in Supporting Information Figure S3a. Figure 4c is a typical HRTEM image of an individual NP. The lattice spacing of the NP was measured to be 0.22 nm, corresponding to the (111) plane of the crystallite. The fast Fourier transform (FFT) of the lattice image indicates that the NP has a fcc structure on its [110] zone axis (Figure 4d). Figure 4e shows an electron diffraction pattern taken from the selected region marked by the circle (Supporting Information Figure S3b). This pattern clearly consists of a number of distinct concentric rings originating from the (111), (200), (220), and (311) planes of the crystal in addition to a (002) reflection from the NCNT.<sup>37</sup> On the basis of the TEM observation, the mean particle diameter for 100 different NPs ( $d_{\text{mean}}$ ) amounts to  $\approx 2.89$  nm, in good agreement with the value derived from the XRD analysis. In addition to ultrafine crystallites, some clusters with size  $\leq 1.5$  nm were also found. Note that the particle size obtained here is even smaller compared with that of Cu, Pt, and Pt–Cu core–shell and alloy NPs stabilized by either oleylamine/oleic acid or polyvinylpyrrolidone.<sup>38</sup> Extracting particle size distribution histograms (Figure 4f) allows us to estimate the relative standard deviation of the particle diameter ( $\text{RSD}_{\text{dia}}$ ), which is equal to 24%, indicating good particle size monodispersity. The surface average dispersion,  $D$ , was estimated to be 39.7% by the

relation based on the Borodzinski and Bonarowska model:  $D = 2.64/(d_{\text{mean}}/d_{\text{at}})^{0.81}$ , using the atomic diameter,  $d_{\text{at}}$ , of Pt (0.278 nm).<sup>39</sup>

The composition of the Pt–Cu NPs can be tuned by controlling the added amount of  $\text{Pt}(\text{NO}_3)_2$ . This also allowed us to tailor the size of the Pt–Cu NPs. For example, the particle size was decreased from  $\approx 3.1$  to  $\approx 2.9$  nm, as the molar ratio of Pt to Cu was increased from 1:3 to 1:1. On the other hand, manipulating the seed particle size also allows us to control the Pt–Cu particle size: increasing the size of the Cu NPs from 9.4 to 11.5 nm resulted in an increase in the Pt–Cu size from 2.89 to 3.0 nm. The size of Cu NPs can be readily tailored by varying their loading level on the NCNTs, ultrasonic intensity, and precursor concentration. The size of the Cu NPs increases with the Cu loading at a given NCNT concentration and can be tuned in the range from 6.2 to 12.2 nm by increasing the Cu loading from 5 to 20 wt %. By altering the precursor concentration while keeping the Cu loading fixed, the size of the Cu NPs was finely tuned, as well. As a control experiment, the size of the Cu particles was reduced from 8.83 to 5.68 nm at  $\approx 7$  wt % Cu loading by decreasing the concentration of  $\text{Cu}(\text{NO}_3)_2 \cdot 3\text{H}_2\text{O}$  from 0.744 to 0.372 mg  $\text{mL}^{-1}$ . This scenario is due to the fact that lesser amounts of  $\text{Cu}^{2+}$  contributed to the growth of the nuclei at lower quantities of precursor addition. Alternatively, as the output ultrasonic intensity was increased from  $6.75 \pm 0.42$  to  $22.1 \pm 1.37$   $\text{W cm}^{-2}$  while keeping the Cu loading and its precursor concentration constant, the size of the Cu NPs decreased by 29.9% to 7.68 nm, as shown in Figure 5. This may be associated with the enhancement of the nucleation rate as a result of more cavitation bubbles being generated by the higher ultrasonic energy.

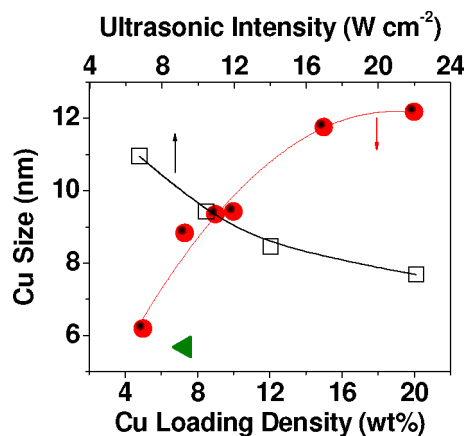


**Figure 5.** Cu particle size as a function of its mass loading level on NCNTs at a given initial NCNT concentration of  $0.125$  mg  $\text{mL}^{-1}$  and ultrasonic intensity of  $10.5 \pm 1.0$   $\text{W cm}^{-2}$  ( $\bullet$ ), and ultrasonic intensity at 10 wt % Cu loading and its precursor concentration of  $1.05$  mg  $\text{mL}^{-1}$  ( $\diamond$ ). The  $\blacktriangleleft$  symbol stands for the particle size in the case of a half precursor concentration at 7 wt % Cu loading and ultrasonic intensity of  $10.5 \pm 1.0$   $\text{W cm}^{-2}$ . The lines are drawn to guide the eye.

To address the question as to whether the nanoparticles are bimetallic in individual NPs or in an ensemble of monometallic NPs, high-angle annular dark-field scanning TEM (HAADF-STEM) coupled with EDX was employed. As shown in Figure 6a, NPs with narrow size distribution are well dispersed on the NCNT support. Multiple single-particle EDX measurements confirmed the bimetallic nature of the particles (Supporting Information Figure S3c, d). Further STEM-EDX line scans

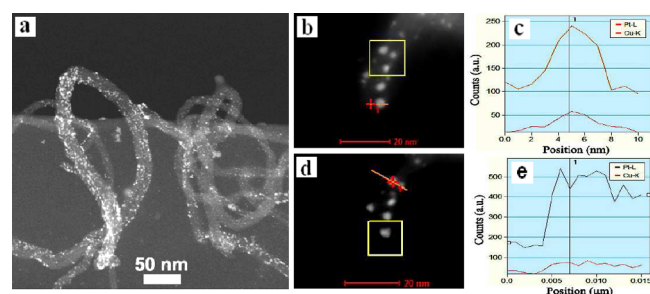


**Figure 6.** (a) Low-magnification and (b, d) high-magnification STEM images of Pt–Cu/NCNTs. (c, e) Drift-corrected line scan profiles from the regions shown in b and d, respectively. The boxed areas in b and d are chosen for drift correction purpose during the line scan. The top line in both c and e shows the counts for Pt, while the bottom line shows the counts for Cu.

from different regions demonstrated the homogeneity in the composition of the NPs. The clear concurrence of both elements may indicate that the major phase of Pt–Cu in the sample is an alloy (Figure 6c), consistent with the XRD results. These results differ from the formation of core–shell Pt@Cu architectures using a sequential reduction strategy<sup>38</sup> or physical mixtures of phase-separated species using a coreduction procedure.<sup>20</sup> Alternatively, a few bimetallic NPs with poorly defined element distribution were also identified (Figure 6d, e), which may be partly attributed to the presence of copper oxide. However, NPs with “Swiss-cheese” structure were not observed. The electron energy loss spectroscopy (EELS) spectrum of the Cu L edge from the region containing several large NPs with size >5 nm illustrates that Cu has a zero oxidation state (Supporting Information Figure S3e).<sup>10</sup>

Three interesting aspects that warrant further exploration were observed in this work. First, displacement of Cu by Pt<sup>2+</sup> under intense sonication resulted in a significant reduction in particle size. Assuming that the number of particles remains constant, a large change in particle size is unlikely to occur because the volume of consumed Cu should be compensated with a similar volume of produced Pt. This is clearly not the case, allowing us to infer that a strong increase in particle number must have occurred during the replacement reaction. The TEM observations offer a direct proof for this deduction, as shown in Figure 7. Obviously, a large number of smaller Pt–Cu NPs were obtained, as opposed to the lower amount of the seed Cu NPs with larger size. In addition, some bare NCNTs free from the deposition of Cu NPs were found to be decorated with the Pt–Cu NPs. Applying a simple sphere model, the number density of Pt–Cu NPs with a Pt/Cu molar ratio at 1:1 should be ~35 times as high as that of the seed Cu NPs (7 wt % Cu loading on NCNTs) prior to the replacement reaction (for details, see the Supporting Information). We also note that the redox reaction even occurred upon addition of Pt(NO<sub>3</sub>)<sub>2</sub> within 10 s under tip sonication, and ultrafine Pt–Cu NPs with size less than 2 nm were obtained (Supporting Information Figure S4a). Last but not least, alloys of Pt–Cu were formed rather than core–shell architectures, as expected.

Two possible explanations may be relevant. On one hand, in addition to the galvanic replacement process occurring between Cu and the Pt<sup>2+</sup> ions in contact with Cu particles, the good conductive nature of NCNTs also enabled electron transfer from Cu to those Pt<sup>2+</sup> interfacing with the surface of NCNTs, allowing their reduction. Electrochemical equilibrium between two dissimilar NPs wired by NCNTs and in equilibrium with

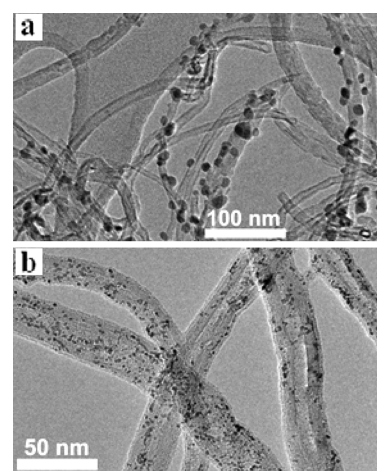


**Figure 7.** TEM images of (a) Cu/NCNTs with 7 wt % Cu loading prior to the redox replacement reaction and (b) Pt–Cu/NCNTs after the displacement of Cu (shown in a) by Pt<sup>2+</sup>.

ionic species in solution can only be maintained when the charge dispensed by dissolution of a metallic species is countered by a reaction consuming the charge. The ultimate consequence of this phenomenon is shrinkage of the size of the Cu NPs and multiplication of the particle number density. On the other hand, we suppose that intense ultrasonication might play a key role in the evolution of the structure.<sup>21–25</sup> Specifically, the mechanical effects of cavitation and shear forces greatly promote the mass transfer of reactants, permitting better wetting of the Cu surfaces with Pt(NO<sub>3</sub>)<sub>2</sub> solution. The redox displacement of Cu by Pt<sup>2+</sup> is assumed to be dramatically accelerated at ≈0 °C by shock waves generated during cavitation with instantaneous temperatures up to 5000 K, pressures in excess of 20 MPa, and rapid heating/cooling rates > 10<sup>9</sup> K s<sup>−1</sup>. The extreme conditions originating from cavitation may favor Pt diffusion into the vacancies of the Cu bulk due to the Kirkendall effect (the diffusion of Pt into Cu is faster relative to Cu diffusion into Pt),<sup>38</sup> thereby facilitating the alloying of Pt with Cu. The alloy species may tend to diffuse out of the Cu interface, forming nuclei as a result of intercollision, and may be preferably deposited onto NCNTs under ultrasonic irradiation. From the sonocrystallization point of view, ultrasonic radiation can induce the primary nucleation at lower supersaturation levels and can also significantly reduce the induction time and metastable zone width. As a consequence, a sharp rise in nuclei population and rate of nucleation may have occurred, presumably as a result of the shock waves, resulting in small particle size. We found that this concept is highly flexible and applicable to the design of a variety of bimetallic NPs, such as Pt–Ag, Pd–Cu Pd–Ag, and Au–Pd NPs (Supporting Information Figure S4b–d).

The resulting Pt–Cu NPs supported on NCNTs with different Pt/Cu molar ratios were applied in the oxygen reduction reaction (ORR). Before the ORR investigations, the catalysts were voltammetrically treated by potential cycling between 0.0 and 1.0 V vs RHE at a scan rate of 100 mV s<sup>−1</sup> in deaerated HClO<sub>4</sub> (0.1 M) (Figure 8a). The initial trace (dotted line in Figure 8a) shows prominent Cu dissolution during the anodic scan between 0.2 and 0.35 V and Cu redeposition (0–0.25 V) during the cathodic scan.<sup>5,40</sup> Characteristic anodic stripping peaks associated with underpotentially deposited hydrogen on Pt surface atoms between 0.04 and 0.4 V were not

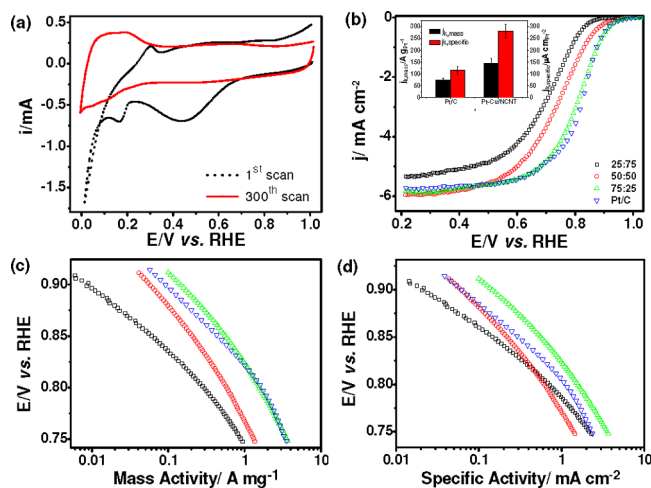


**Figure 8.** (a) Voltammetric pretreatment of the Pt–Cu/NCNT catalyst by potential cycling between 0.0 and 1.0 V vs RHE in deaerated HClO<sub>4</sub> (0.1 M) at a scan rate of 100 mV s<sup>-1</sup>. (b) Comparison of thin-film RDE polarization curves for O<sub>2</sub> reduction using the Pt–Cu/NCNT catalysts with varying molar ratio of Pt to Cu (□, 25:75; ○, 50:50; △, 75:25) and the Pt/C reference catalyst (▽). The inset shows mass- and area-specific activities of the Pt–Cu/NCNT (Pt/Cu = 75:25) and Pt/C catalysts at 0.9 V. Mass-transport-corrected Tafel plots of (c) Pt mass-based activity and (d) Pt surface-area-based activity of the catalysts.

clearly discernible. This may be an indication of Cu surface segregation in Cu-rich Pt–Cu alloys.<sup>41</sup> Cu dissolution decayed to undetectable levels after 10 cycles, while hydrogen adsorption and desorption started to manifest and increased gradually in intensity with further potential cycling. After dealloying over ~300 cycles, the cyclic voltammogram reached a steady state resembling that of pure Pt (solid line in Figure 8a). On the basis of previous studies regarding the dealloying of bimetallic catalysts,<sup>42,43</sup> we suppose that a disordered or roughened “Pt skeleton” structure was probably formed as Cu selectively dissolved from the surface or subsurface layers of the Pt–Cu NPs.

To unravel the correlation of their electrocatalytic behavior with the molar ratio of Pt/Cu, NCNT-supported Pt–Cu NPs with three different Pt/Cu molar ratios (Pt/Cu = 25:75, 50:50, and 75:25) were applied in the ORR in acidic electrolyte. Figure 8b shows a comparison of linear sweep voltammograms of the catalysts recorded at a rotation speed of 1600 rpm in oxygen-saturated 0.1 M HClO<sub>4</sub>. Detailed results for electrochemical characterization of the three catalysts together with the commercial Pt-E-TEK (20% Pt on Vulcan carbon) are summarized in Table 1: both the electrochemical surface area and the ORR activity of the Pt–Cu/NCNT catalysts showed a monotonic increase with increasing Pt/Cu molar ratio in the

range from 25:75 to 75:25. When the ratio of Pt/Cu was less than 25:75, Pt-like features were either imperceptible or poorly developed, even after several hundred voltammetric pretreatment cycles, and the corresponding ORR activity was very low. The measured overpotential for the ORR was 88 and 44 mV higher for Pt/Cu (25:75) and Pt/Cu (50:50), respectively, compared with Pt/Cu (75:25) at a current density of 1 mA cm<sup>-2</sup>. In particular, the mass- and area-specific activities of the as-obtained Pt–Cu catalyst (Pt/Cu = 75:25) were 1.72 and 2.57 times as high as those for the standard Pt/C commercial catalyst tested under similar conditions, respectively.

To gain a deeper insight into the origin of the activity differences, the intrinsic activities of the catalysts were expressed by means of Tafel plots, for which the kinetic currents were corrected for mass-transport effects (Figure 8c, d). Both the mass- and area-specific activities of the Pt–Cu/NCNT (Pt/Cu = 75:25) catalyst are superior to those of the reference catalyst at potentials above 0.85 V. The exact origin of the activity enhancement for Pt-based catalysts is still a subject of ongoing discussion related to electronic (ligand) and geometric effects.<sup>1,10</sup> From an electronic effect point of view, modification of the electronic properties of Pt by the less noble metal can reduce the chemisorption energy of oxygenated species on Pt, thereby maximizing the utilization of Pt active sites.<sup>40,44</sup> On the basis of the geometric mechanism including lattice-induced strain effects as well as Pt particle size effects, doping Pt with a second metal may enable the contraction of the interatomic distance between Pt atoms (Pt–Pt) in the surface layer/ resulting in an enhancement of its ORR activity.<sup>45</sup>

## CONCLUSIONS

Well dispersed bimetallic Pt–Cu alloy NPs with high uniformity in size and composition were synthesized on NCNTs at *T* ≈ 0 °C on the basis of the displacement of Cu by Pt<sup>2+</sup> under high-intensity sonication. The process is considered efficient, simple, and environmentally friendly, requiring no capping ligand or electrochemical treatments. Adjusting the added amount of Pt(NO<sub>3</sub>)<sub>2</sub> permitted tuning the size and composition of the bimetallic NPs. The size of the Pt–Cu NPs was also found to depend on the seed Cu particle size, which was controlled by the Cu loading level on the NCNTs, the ultrasonic intensity, and the concentration of Cu(NO<sub>3</sub>)<sub>2</sub>·3H<sub>2</sub>O. The resulting Pt–Cu/NCNT catalyst exhibited an enhanced electrocatalytic activity in the oxygen reduction reaction compared with a commercial Pt/C catalyst.

## ASSOCIATED CONTENT

### Supporting Information

Scheme of the sonochemical system; Pt 4f and Cu 2p core level XPS spectra of Pt–Cu/NCNT; TEM images of Cu/NCNTs,

**Table 1. Electrochemically Active Surface Area (ECSA) and ORR Activity of Pt–Cu/NCNTs with Varying Pt/Cu Molar Ratios and Pt-E-TEK (20% Pt on Vulcan Carbon)**

catalyst Pt/Cu	ECSA	activity			
		mass activity (A/g <sub>Pt</sub> )		specific activity (μA/cm <sup>2</sup> )	
		0.85 V	0.9 V	0.85 V	0.9 V
25:75	21.4 ± 3.2	44 ± 6		76 ± 11	
50:50	37.2 ± 7.6	163 ± 11	56 ± 7	237 ± 27	125 ± 24
75:25	44.1 ± 3.9	432 ± 23	146 ± 21	572 ± 31	282 ± 29
Pt-E-TEK	61.0 ± 4.1	329 ± 9	74 ± 8	316 ± 23	116 ± 17

Pt–Cu/NCNTs, Pd–Cu/NCNT, Pd–Ag/NCNT, and Au–Pd/NCNT; quantitative SEM-EDX analysis; STEM-EDX pattern; EELS Cu spectrum of Pt–Cu/NCNTs. This information is available free of charge via the Internet at <http://pubs.acs.org/>.

## AUTHOR INFORMATION

### Corresponding Author

\*Phone: +49(0)234 32-28754. Fax: +49(0)234 32-14115. E-mail: [muhler@techem.rub.de](mailto:muhler@techem.rub.de).

### Notes

The authors declare no competing financial interest.

## ACKNOWLEDGMENTS

Zhenyu Sun thanks the Alexander von Humboldt Foundation for an experienced researcher fellowship. Justus Masa is grateful to the Germany Academic Exchange Service (DAAD) for a Ph.D. scholarship.

## REFERENCES

- (1) Stamenkovic, V. R.; Fowler, B.; Mun, B. S.; Wang, G. F.; Ross, P. N.; Lucas, C. A.; Markovic, N. M. *Science* **2007**, *315*, 493–497.
- (2) Koh, S.; Leisch, J.; Toney, M. F.; Strasser, P. *J. Phys. Chem. C* **2007**, *111*, 3744–3752.
- (3) Greeley, J.; Stephens, I. E. L.; Bondarenko, A. S.; Johansson, T. P.; Hansen, H. A.; Jaramillo, T. F.; Rossmeisl, J.; Chorkendorff, I.; Norskov, J. K. *Nat. Chem.* **2009**, *1*, 552–556.
- (4) Lim, B.; Jiang, M.; Camargo, P. H. C.; Cho, E. C.; Tao, J.; Lu, X. M.; Zhu, Y. M.; Xia, Y. N. *Science* **2009**, *324*, 1302–1305.
- (5) Gupta, G.; Slanac, D. A.; Kumar, P.; Wiggins-Camacho, J. D.; Wang, X. Q.; Swinnea, S.; More, K. L.; Dai, S.; Stevenson, K. J.; Johnston, K. P. *Chem. Mater.* **2009**, *21*, 4515–4526.
- (6) Peng, Z. M.; You, H. J.; Yang, H. *Adv. Funct. Mater.* **2010**, *20*, 3734–3741.
- (7) Kim, Y.; Hong, J. W.; Lee, Y. W.; Kim, M.; Kim, D.; Yun, W. S.; Han, S. W. *Angew. Chem., Int. Ed.* **2010**, *49*, 10197–10201.
- (8) Peng, Z. M.; Wu, J. B.; Yang, H. *Chem. Mater.* **2010**, *22*, 1098–1106.
- (9) Mazumder, V.; Chi, M. F.; More, K. L.; Sun, S. H. *Angew. Chem., Int. Ed.* **2010**, *49*, 9368–9372.
- (10) Dutta, I.; Carpenter, M. K.; Balogh, M. P.; Ziegelbauer, J. M.; Moylan, T. E.; Atwan, M. H.; Irish, N. P. *J. Phys. Chem. C* **2010**, *114*, 16309–16320.
- (11) Xu, J. G.; Wilson, A. R.; Rathmell, A. R.; Howe, J.; Chi, M. F.; Wiley, B. J. *ACS Nano* **2011**, *5*, 6119–6127.
- (12) Koenigsmann, C.; Santulli, A. C.; Gong, K.; Vukmirovic, M. B.; Zhou, W. P.; Sutter, E.; Wong, S. S.; Adzic, R. R. *J. Am. Chem. Soc.* **2011**, *133*, 9783–9795.
- (13) Yong, H. *Angew. Chem., Int. Ed.* **2011**, *50*, 2674–2676.
- (14) Mayrhofer, K. J. J.; Arenz, M. *Nat. Chem.* **2009**, *1*, 518–519.
- (15) Kammler, H. K.; Madler, L.; Pratsinis, S. E. *Chem. Eng. Technol.* **2001**, *24*, 583–596.
- (16) Eliezer, S.; Eliaz, N.; Grossman, E.; Fisher, D.; Gouzman, I.; Henis, Z.; Pecker, S.; Horovitz, Y.; Fraenkel, M.; Maman, S.; Lereah, Y. *Phys. Rev. B* **2004**, *69*, 144119.
- (17) Lin, P. A.; Sankaran, R. M. *Angew. Chem., Int. Ed.* **2011**, *50*, 10953–10956.
- (18) Zhang, J. L.; Vukmirovic, M. B.; Xu, Y.; Mavrikakis, M.; Adzic, R. R. *Angew. Chem., Int. Ed.* **2005**, *44*, 2132–2135.
- (19) Zhang, J. L.; Vukmirovic, M. B.; Sasaki, K.; Nilekar, A. U.; Mavrikakis, M.; Adzic, R. R. *J. Am. Chem. Soc.* **2005**, *127*, 12480–12481.
- (20) Tao, F.; Grass, M. E.; Zhang, Y. W.; Butcher, D. R.; Renzas, J. R.; Liu, Z.; Chung, J. Y.; Mun, B. S.; Salmeron, M.; Somorjai, G. A. *Science* **2008**, *322*, 932–934.
- (21) Suslick, K. S.; Choe, S. B.; Cichowlas, A. A.; Grinstaff, M. W. *Nature* **1991**, *353*, 414–416.
- (22) Cravotto, G.; Cintas, P. *Chem. Soc. Rev.* **2006**, *35*, 180–196.
- (23) Ohayon, E.; Gedanken, A. *Ultrason. Sonochem.* **2010**, *17*, 173–178.
- (24) Pollet, B. G. *Int. J. Hydrogen Energy* **2010**, *35*, 11986–12004.
- (25) Pollet, B. G. *Electrochem. Commun.* **2009**, *11*, 1445–1448.
- (26) Sun, Z. Y.; Nicolosi, V.; Rickard, D.; Bergin, S. D.; Aherne, D.; Coleman, J. N. *J. Phys. Chem. C* **2008**, *112*, 10692–10699.
- (27) Xia, W.; Chen, J.; Kundu, S.; Muhler, M. *Carbon* **2009**, *47*, 919–922.
- (28) Kundu, S.; Xia, W.; Busser, W.; Becker, M.; Schmidt, D. A.; Havenith, M.; Muhler, M. *Phys. Chem. Chem. Phys.* **2010**, *12*, 4351–4359.
- (29) Sun, Y. G.; Mayers, B. T.; Xia, Y. N. *Nano Lett.* **2002**, *2*, 481–485.
- (30) Liang, H. P.; Zhang, H. M.; Hu, J. S.; Guo, Y. G.; Wan, L. J.; Bai, C. L. *Angew. Chem., Int. Ed.* **2004**, *43*, 1540.
- (31) Xu, C. X.; Wang, L. Q.; Wang, R. Y.; Wang, K.; Zhang, Y.; Tian, F.; Ding, Y. *Adv. Mater.* **2009**, *21*, 2165–2169.
- (32) LaCroix, L. B.; Shadle, S. E.; Wang, Y. N.; Averill, B. A.; Hedman, B.; Hodgson, K. O.; Solomon, E. I. *J. Am. Chem. Soc.* **1996**, *118*, 7755–7768.
- (33) Sun, Z. Y.; Liu, Z. M.; Han, B. X.; Wang, Y.; Du, J. M.; Xie, Z. L.; Han, G. J. *Adv. Mater.* **2005**, *17*, 928–932.
- (34) Vegard, L. Z. *Phys.* **1921**, *5*, 17–26.
- (35) Sun, Z. Y.; Zhao, Y. F.; Xie, Y.; Tao, R. T.; Zhang, H. Y.; Huang, C. L.; Liu, Z. M. *Green Chem.* **2010**, *12*, 1007–1011.
- (36) Wu, C. K.; Yin, M.; Brien, S. O.; Koberstein, J. T. *Chem. Mater.* **2006**, *18*, 6054–6058.
- (37) Liu, L. F.; Pippel, E. *Angew. Chem.* **2011**, *123*, 2781–2785.
- (38) Zhou, S. H.; Varughese, B.; Eichhorn, B.; Jackson, G.; McIlwrath, K. *Angew. Chem., Int. Ed.* **2005**, *44*, 4539–4543.
- (39) Borodziński, A.; Bonarowska, M. *Langmuir* **1997**, *13*, 5613–5620.
- (40) Mani, P.; Srivastava, R.; Strasser, P. *J. Phys. Chem. C* **2008**, *112*, 2779–2778.
- (41) Ruban, A. V.; Skriver, H. L.; Norskov, J. K. *Phys. Rev. B* **1999**, *59*, 15990–16000.
- (42) Stamenkovic, V. R.; Mun, B. S.; Mayrhofer, K. J. J.; Ross, P. N.; Markovic, N. M. *J. Am. Chem. Soc.* **2006**, *128*, 8813–8819.
- (43) Zhang, J.; Lima, F. H.; Shao, M. H.; Sasaki, K.; Wang, J. X.; Hanson, J.; Adzic, R. R. *J. Phys. Chem. B* **2005**, *109*, 22701–22704.
- (44) Sarkar, A.; Manthiram, A. *J. Phys. Chem. C* **2010**, *114*, 4725–4732.
- (45) Strasser, P.; Koh, S.; Anniyev, T.; Greeley, J.; More, K.; Yu, C.; Liu, Z.; Kaya, S.; Nordlund, D.; Ogasawara, H.; Toney, M. F.; Nilsson, A. *Nat. Chem.* **2010**, *2*, 454–460.